# An Analytical Electron Microscope Investigation of the Phase Transformations in a Simulated Heat-Affected Zone in Alloy 800

A. D. ROMIG, Jr., J. C. LIPPOLD, and M. J. CIESLAK

The heat-affected zone (HAZ) hot-cracking behavior of Alloy 800 was investigated with hot ductility (Gleeble) testing during a simulated HAZ thermal cycle. Microstructural analyses were performed by optical metallography, fractography, electron microprobe analysis, and analytical electron microscopy on specimens that were water quenched from selected temperatures during this thermal cycle. Analysis of analytical electron microscopy (AEM) and Auger electron spectroscopy (AES) data suggests that incipient melting of the grain boundaries occurs at temperatures of 1300 °C and above. The HAZ hot-cracking mechanism was consistent with aspects of a constitutional liquation phenomenon involving a nonequilibrium eutectic-type reaction between grain boundary Ti(C, N) and the austenitic matrix. The extent of expected HAZ cracking would be low as the liquation of Ti(C, N) was localized and no lower melting intermetallic solidification products (*e.g.*, Laves) were observed. The mechanistic observations were consistent with classical thermodynamic and solid state diffusion models.

## I. INTRODUCTION

ALLOY 800 is a fully austenitic Fe-Ni-Cr stainless steel which provides a combination of strength and corrosion resistance at temperatures up to 650 °C. Alloy 800 was originally developed as a heater element sheath material in electrical appliances, but more recently, it has been utilized as a structural material in high temperature components. For example, Alloy 800 tubing has been used extensively in heat exchangers for both conventional and nuclear power plants. Since welding is an important fabrication step in the implementation of any structural alloy, considerable attention has been focused on the weld cracking susceptibility of Alloy 800.

### A. *Heat-Affected Zone Cracking*

Heat-affected zone (HAZ) cracking susceptibility is a problem which plagues many of the highly alloyed austenitic stainless steels and nickel-based superalloys. Fusion zone cracking is also encountered in these materials but is usually avoided by the selection of appropriate weld filler materials. HAZ cracking is more insidious, since the phenomenon is often related to the composition of the material and its microstructure, both of which have been optimized to achieve desirable base metal properties.

Several investigators have studied HAZ cracking in Alloy 800 weldments.[1–4] In general, the HAZ cracking was restricted to grain boundaries adjacent to the fusion line and appeared to result from localized melting along these boundaries at temperatures slightly below the bulk solidus temperature.[1,4] Electron probe microanalysis (EPMA) of these liquated boundaries revealed a nearly 50-fold increase in Ti content[4] relative to the average alloy composition (in wt pct: 46Fe-32.5Ni-21Cr-0.38Cu-0.38Al-0.38Ti-0.05C-0.008S).[5]

Several mechanisms have been proposed to explain the HAZ hot cracking phenomenon.[4,6–12] One mechanism involves the segregation of minor elements or impurities to the grain boundary, leading to a localized composition with a low melting point.[13] If the impurity is present in the matrix as a supersaturated solution and given sufficient time at temperature, the impurity will segregate to the grain boundary, the segregation being driven by a chemical potential gradient toward the grain boundary. If there is insufficient time for the elements to diffuse to the boundary, a moving boundary may sweep up the impurity through a "grain boundary sweeper" mechanism. In the case of Alloy 800, if the grain boundaries become enriched in Ti, either through volume diffusion or a grain boundary sweeper, one might postulate melting at the grain boundaries *via* the Fe-Ti and/or Ni-Ti eutectic reactions.

Alternatively, a "constitutional liquation" mechanism has also been used to explain HAZ cracking in several nickel-base alloys,[7,8,9] high alloy stainless steels,[11] and maraging steel.[6] Fundamentally, this involves the melting of compounds (carbides, nitrides, *etc.*) in a region of the HAZ which is rapidly heated to near solidus temperatures. The rapid heating rates are such that complete dissolution of these compounds does not occur instantaneously above their solvus temperatures. The remaining compounds undergo a eutectic-type liquation reaction with the surrounding matrix at some higher critical temperature. As simultaneous grain growth occurs, the migrating grain boundaries encounter the liquated particles and are subsequently wetted by the liquid phase, rendering the microstructure susceptible to cracking. The mechanism proposed in this work is a variation of the "constitutional liquation" mechanism in which the compound, Ti(C, N), already present at the grain boundaries liquates in a eutectic-type reaction with the surrounding austenitic matrix.

Isothermal transformations, occurring under no applied stress, in Ti-stabilized and Nb-stabilized Fe-20 wt pct Cr-25 wt pct Ni alloys have been studied by Adamson *et al.*[14] For alloys containing less than 1 wt pct Ti, a liquation reaction resulting in the formation of an intermetallic constituent (Laves–$M_2Ti$) was not observed during extended (>1 hour) heat treatments at 1350 °C. For alloys containing more than 1 wt pct Ti, a grain boundary precipitate phase is observed after 2.5 hours at 1350 °C. The authors stated that identification of these precipitates with electron diffraction was not possible, but the chemical analysis suggested a Ti-rich Laves phase.

A. D. ROMIG, Jr., Physical Metallurgy, and M. J. CIESLAK, Process Metallurgy, are with Sandia National Laboratories, Albuquerque, NM 87185. J. C. LIPPOLD is with Edison Welding Institute, Columbus, OH.

Manuscript submitted May 9, 1986.

In the same study, alloys containing as little as 0.16 wt pct Nb were observed to undergo a liquation transformation at 1350 °C resulting in the formation of a Laves constituent ($M_2Nb$). In this case, the Laves arose from the dissolution products of NbC. The results of this study revealed that the liquation sensitivity and transformation kinetics which result in Laves phase formation are strong functions of stabilizer chemistry, both in terms of the specific stabilizer present (Nb or Ti) and in the case of Ti, the absolute amount in the alloy. Time at temperature was also an important variable, especially when Ti was the stabilizer. Neither these results,[14] nor those of the present study, address the question of Laves phase formation in the fusion zone where nonequilibrium solidification segregation effects need to be considered.

Laves phase has been identified[11,15] in alloys such as A-286 (Fe-15 wt pct Cr-25 wt pct Ni-2.2 wt pct Ti-1.2 wt pct Mo) which contain up to half an order of magnitude more Ti than found in Alloy 800. In the same study,[11] it was observed that HAZ hot cracking could be modified by variations in Ti content. That is, when the Ti content was increased from the nominal (2.22 wt pct) to 2.63 wt pct, the hot cracking susceptibility was dramatically increased. Conversely, when the Ti content was lowered to 1.6 wt pct, no HAZ hot cracking was observed. The presence of Laves in the 1.6 wt pct Ti alloy was not explicitly reported.[11]

### B. *Analytical Electron Microscopy*

X-ray microanalysis in the electron probe microanalyzer (EPMA) and more recently the analytical electron microscope (AEM) have become powerful tools for the investigation of elemental segregation in engineering materials.[16–19] The salient characteristic of the EPMA and AEM is the ability to determine the chemical composition of very small volumes of the sample. With the EPMA, one can measure composition of precipitates, in a matrix, as small as 1 $\mu$m in diameter. Since the electron scattering volume in a thin foil is far smaller than in a bulk target,[20] the composition of small precipitates less than 50 nm in diameter can be measured by the AEM. Due to the smaller scattering volume in thin foils, it is also possible with the AEM to measure concentration profiles (less than 1 $\mu$m in length) which develop at interfaces during liquid-solid and solid-solid phase transformations. The factor of twenty improvement in X-ray spatial resolution in the AEM relative to the EPMA has provided the ability to measure the composition of small precipitates and to detect elemental segregation at interphase boundaries and grain boundaries with a spatial level totally unattainable in the EPMA.

## II. EXPERIMENTAL PROCEDURE

### A. *Material*

The Alloy 800 used in this investigation was obtained in the form of 25 × 100 mm bar stock. The composition of the material (in weight percent) was 19.55Cr, 32.47Ni, 0.93Mn, 0.08Si, 0.49Ti, 0.40Al, 0.71Cu, 0.08C, 0.018N, 0.004S, 0.008P, 0.05Nb, and the balance Fe. The material was in the mill-annealed condition. Mill annealing of Alloy 800 is normally performed in the temperature range from 980 to 1000 °C for typically 15 minutes. This heat treatment produces a microstructure which is fully austenitic and exhibits a grain size in the range ASTM 8 to 12. An optical micrograph of this microstructure is shown in Figure 1. The mill-annealing treatment lies in the carbide precipitation temperature range and results in the precipitation of both M(C, N) and $M_{23}C_6$ type carbides and carbonitrides.[21] These are the fine precipitates evident in Figure 1. Large, blocky TiN particles are also present in the microstructure. These nitrides are remnants of the original solidification processing of the ingot.

### B. *Hot Ductility Testing*

During welding, the temperature gradient from the weld fusion line into the adjacent HAZ can be extremely steep. As a consequence, significant microstructural variation in the HAZ can occur over a short distance. For instance, the region of the HAZ in Alloy 800 weldments in which liquation cracking is observed extends approximately 0.15 mm from the fusion line.[4] It is often desirable to produce bulk samples which simulate specific regions in the HAZ in order to facilitate the analysis of these microstructures. The Gleeble has been specifically developed to simulate the HAZ of welds and is capable of precisely controlled heating and cooling profiles characteristic of specific HAZ regions. The Gleeble thermomechanical testing apparatus[22] was used in this investigation to study the evolution of the hot crack susceptible microstructure in the HAZ of Alloy 800. Reported temperatures for the Gleeble experiments are accurate to better than 2 pct.

The Gleeble samples used in this investigation were machined from the as-received Alloy 800 bar stock and were nominally 6.35 mm in diameter and 100 mm in length. These samples were heated in the Gleeble to simulate the on-heating and on-cooling behavior of the microstructure adjacent to the fusion line. The thermal cycle is shown schematically in Figure 2. At the predetermined points indicated along this cycle, individual samples were pulled to failure. These hot tensile tests (often referred to as hot ductility tests) were performed in vacuum ($5 \times 10^{-4}$ torr) at an extension rate of 40 cm/sec. Duplicate samples were

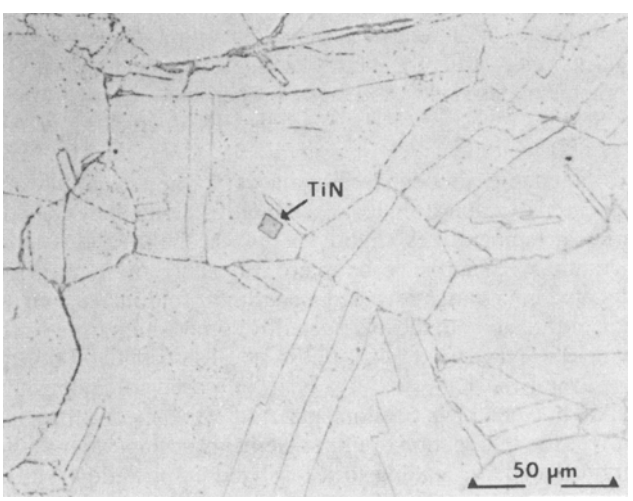


Fig. 1 — Alloy 800 microstructure in the mill-annealed condition, mixed acid etch. The large blocky precipitates are TiN. The small intragranular precipitates are (Nb, Ti)C and (Nb, Ti) (C, N). The grain boundary precipitates are Ti(C, N) and Cr-rich $M_{23}C_6$.

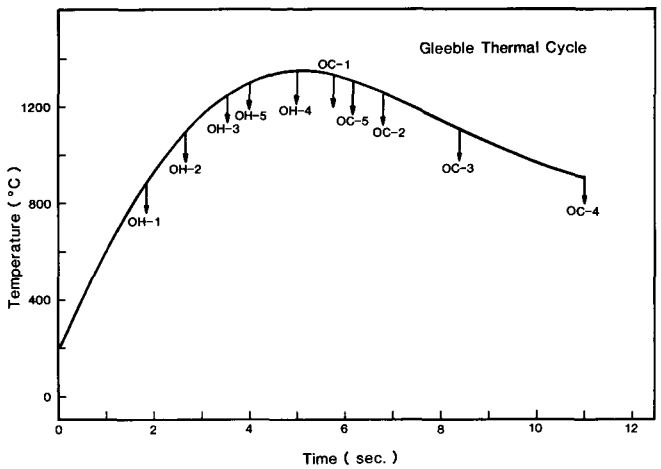


Fig. 2 — Gleeble thermal profile used to simulate the evolution of the HAZ in Alloy 800. Arrows on the curve indicate test temperatures from both the on-heating (OH) and on-cooling (OC) portion of the profile.

quenched in the Gleeble at identical points along the thermal profile by using a water spray quench.

### C. *Analytical Techniques*

The Gleeble samples were mounted for metallographic evaluation and etched with a mixed acid reagent consisting of equal parts nitric, acetic, and hydrochloric acid to reveal the microstructure. EPMA was performed on these samples with a Cameca MBX electron microprobe operated at 15 kV with a beam current of 22 nA. Under these conditions the volume of X-ray generation would be slightly less than 1 $\mu$m in diameter.[23] These conditions were chosen to optimize the spatial resolution of the EPMA analyses. In the current study, the EPMA was used for elemental mapping and qualitative identification of the larger precipitates as nitrides, carbides, or carbonitrides. The poor spatial resolution of the EPMA, relative to the AEM, precluded its use for quantitative investigations of elemental segregation. Hence, all detailed elemental segregation studies were performed by AEM.

Specimens for AEM evaluation were sliced from the Gleeble quench samples with a slow speed diamond saw. After grinding to 125 $\mu$m, 3 mm discs were mechanically punched from the specimens. These discs were electrojet thinned in 10 pct perchloric acid (in methanol) at 15 V and −70 °C. Final cleaning was performed by ion milling.

A JEOL 100C analytical electron microscope equipped with a side-entry EDS detector and a Tracor-Northern TN2000 multichannel analyzer were used to examine the thin foil specimens. The AEM was operated at 100 kV. A nominal beam diameter of 18 nm was used for measuring the composition of the precipitates and measuring concentration profiles across the grain boundaries. To optimize the spatial resolution of the analysis and X-ray counting statistics, all quantitative analyses were performed in regions approximately 50 nm thick (unless otherwise specified). Very thin regions of the foil were deliberately used for the AEM analysis to obtain the best possible spatial resolution. Foil thickness was determined by using the contamination spot technique.[24] The resulting X-ray spatial resolution was approximately 30 nm. At least 5000 counts were collected in the characteristic X-ray peak of interest. When profiling across a grain boundary, the specimen was oriented so that the grain boundary was parallel to the incident electron beam.

The X-ray data were converted into weight percents with the Cliff-Lorimer ratio technique[25] as given by:

$$C_A/C_B = k_{AB}(I_A/I_B) \quad [1]$$

where $C_A$ and $C_B$ are the weight percents of $A$ and $B$, respectively, $k_{AB}$ is a compositionally independent sensitivity factor, and $I_A$ and $I_B$ are background corrected characteristic X-ray intensities. In the present study, quantitative analyses for Fe, Ni, Cr, Ti, and Nb were performed. Four uncoupled expressions of the form given by Eq. [1] can be written. In each expression, the minor element is ratioed against Fe. A constraining equation arises since the sum of the components must total to unity. In these experiments, the values of $k_{AB}$ were determined from standards of known composition in the same instrument used for the examination of experimental specimens. Equation [1] is valid if the thin film criterion is satisfied and the X-ray absorption and fluorescence effects can be neglected.[20] All analyses were performed in regions of the foil which satisfied the thin film criterion. For further detail on the X-ray analysis of thin foils by AEM and the experimental determination of $k_{AB}$ sensitivity factors, the reader is referred to the literature.[16–20,23–26]

## III. RESULTS

### A. *Hot Ductility Behavior*

The hot ductility behavior of Alloy 800 in the temperature range from 900 to 1350 °C is represented by the reduction in area (RA) of the fracture surface *vs* test temperature relationship shown in Figure 3. Note that both the on-heating and on-cooling ductility at a given temperature are shown. As shown on Figure 2, on-cooling specimens were pulled after heating through a peak temperature of 1350 °C. In the on-heating portion of the hot ductility cycle the ductility decreases rapidly at temperatures above approximately 1250 °C. As described by Weiss *et al.*,[27] the observed rapid loss in ductility may be associated with the onset of liquation in the microstructure, a large increase in grain size, or the dissolution of precipitates. As the temperature is increased to 1300 °C and above, liquation does occur. As the temperature increases, the extent of liquation increases and the ductility decreases until the nil-ductility temperature (~1350 °C) is reached.

On-cooling hot ductility behavior is a measure of the rate of recovery of the material after heating through the nil-ductility temperature (1350 °C). Note that the reductions in area on-cooling are offset by approximately 25 °C from those data on-heating, suggesting only a minor effect of exposure to the nil-ductility temperature. The reduction in area data are also consistent with the failure stress data in that the on-cooling and on-heating data are virtually identical.

The magnitude of the temperature range over which ductility drops on the on-heating portion of the curve and recovers on the on-cooling portion of the curve is an approximate measure of the HAZ cracking susceptibility of the

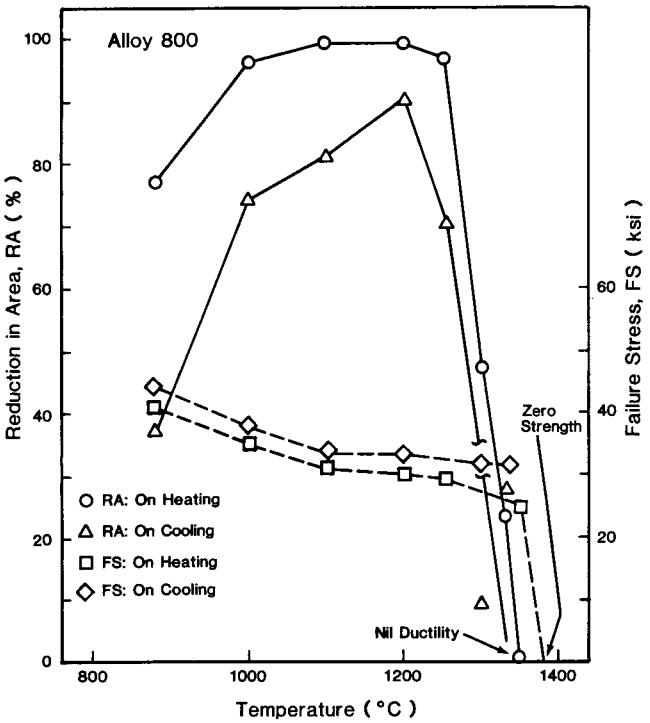


Fig. 3 — The hot ductility behavior of Alloy 800. Samples are heated along the HAZ thermal profile shown in Fig. 2 and tested on either on-heating or on-cooling as indicated.

material.[27,28] The wider the temperature range over which the loss in ductility occurs, the more susceptible the material is to HAZ hot-cracking. In this case, the loss in ductility occurs over the approximate temperature range 1250 °C to 1350 °C. The range is relatively narrow, indicating that Alloy 800 is not extremely sensitive to HAZ hot cracking. The hot ductility results shown in Figure 3 suggest that regions of the Alloy 800 HAZ which are heated above approximately 1300 °C (on-heating) would be susceptible to liquation cracking.

## B. *Fractography*

Evaluation of the fracture characteristics of the hot ductility samples was useful in determining both the onset of liquation during the on-heating portion of the curve and the rate of recovery upon cooling from the peak temperature as shown in Figure 3. Three modes of fracture were observed. In the temperature range between 900 °C and 1250 °C on-heating and between 900 °C and 1200 °C on-cooling, failure was primarily by ductile rupture. Above 1300 °C (either on-heating or on-cooling from 1350 °C) failure was intergranular. In the intermediate temperature ranges, the fracture surfaces exhibited an unusual "spongy" appearance which had both ductile rupture and intergranular characteristics. Fractographs typical of each of these failure types are shown in Figure 4.

## C. *Optical Metallography*

Metallographic examination of the samples from various temperatures along the thermal cycle shown in Figure 2 revealed a significant variation in microstructure during the on-heating portion of the curve. The micrographs shown in Figure 5 reveal the extent of this variation. In the initial portion of the on-heating curve, in the range 900 °C to 1200 °C, there is little apparent change from the original mill-annealed microstructure. Note that the microstructure in Figure 5(a), quenched from 1100 °C, exhibits considerable intergranular carbide precipitation and a grain size comparable to that of the base metal microstructure as shown in Figure 1. At 1250 °C on-heating (Figure 5(b)), an increase in grain size is concomitant with carbide dissolution. Finally, the sample quenched from the peak temperature (1350 °C, Figure 5(c)) exhibits a considerable increase in grain size relative to the starting microstructure. The small grain boundary carbides appear to have dissolved, although remnants of some of these particles are present as small pits throughout the microstructure. The large, blocky TiN particles are relatively unaffected by the thermal cycle.

Despite the dramatic decrease in ductility at temperatures above 1250 °C on-heating, there is no evidence of grain boundary liquation from this temperature range (Figures 5(b), (c)). If the loss in ductility is due to the initial stages of liquation, it is likely that liquid films along grain boundaries are extremely thin and essentially undetectable with optical metallographic techniques. The loss in ductility may be due to increased grain size or precipitate dissolution, both of which are visible in the optical micrographs. Some intergranular liquation at prior grain boundaries was evident, however, upon examination of samples quenched from the on-cooling portion of the curve. These grain boundary features are indicated in Figure 5(d) for a sample quenched from 1325 °C. Note that the remnants of liquation are discrete and do not represent the degree of grain boundary coverage which would explain the complete intergranular failure which occurs at this temperature.

## D. *AEM Results*

### 1. *Mill-annealed microstructure*

Several different types of carbides and carbonitrides were observed in the mill-annealed material. The stability, and in some cases the ultimate temperature of dissolution and/or melting, of these precipitates during the thermal cycle is the key to understanding the mechanism of grain boundary liquation. Hence, the precipitate distribution in the original material must be thoroughly characterized.

A transmission electron microscope (TEM) micrograph of the mill-annealed microstructure is shown in Figure 6. At high magnification, numerous types of carbides and carbonitrides are evident. The grain interior matrix contained numerous small (Nb, Ti)C and (Nb, Ti)(C, N) carbides and carbonitrides, as shown in Figure 6(a). Qualitative X-ray microanalysis in the EPMA demonstrated that both (Nb, Ti)C and (Nb, Ti)(C, N) were present. The precipitates were several hundred nm in diameter, which is too small for quantitative analysis by EPMA, but large enough to detect the presence of Nb, Ti, C, and N by X-ray mapping. The Ti content in the (Nb, Ti)C and (Nb, Ti)(C, N) was exceedingly small. The measured X-ray counts for Ti above background were just above the detectability limit for thin foil analysis in the AEM, which suggests that in this case the Ti content of these carbides and carbonitrides is between 0.5 and 1.0 wt pct Ti. These carbides and carbonitrides were generally irregular in shape with an average diameter of 100 to 200 nm. The (Nb, Ti)C and (Nb, Ti)(C, N) precipitates may

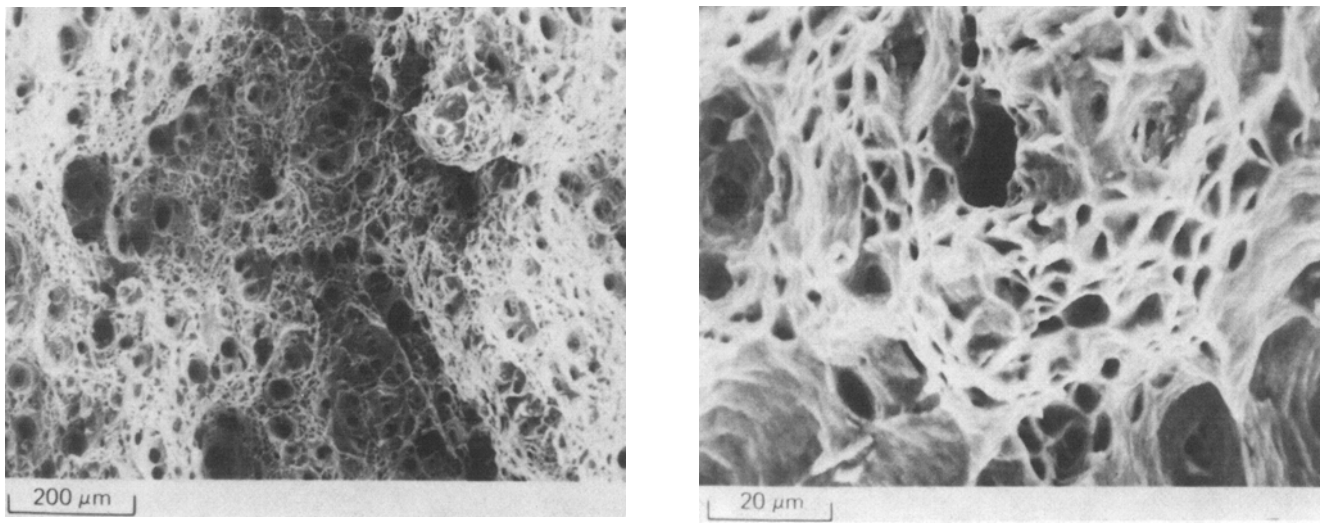


(*a*)

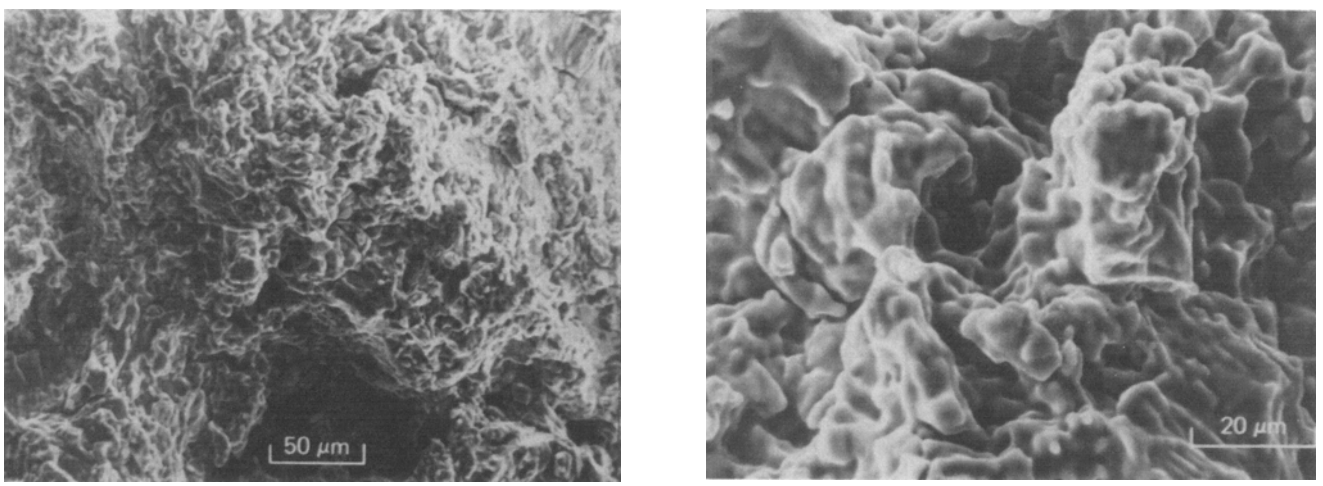


(*b*)

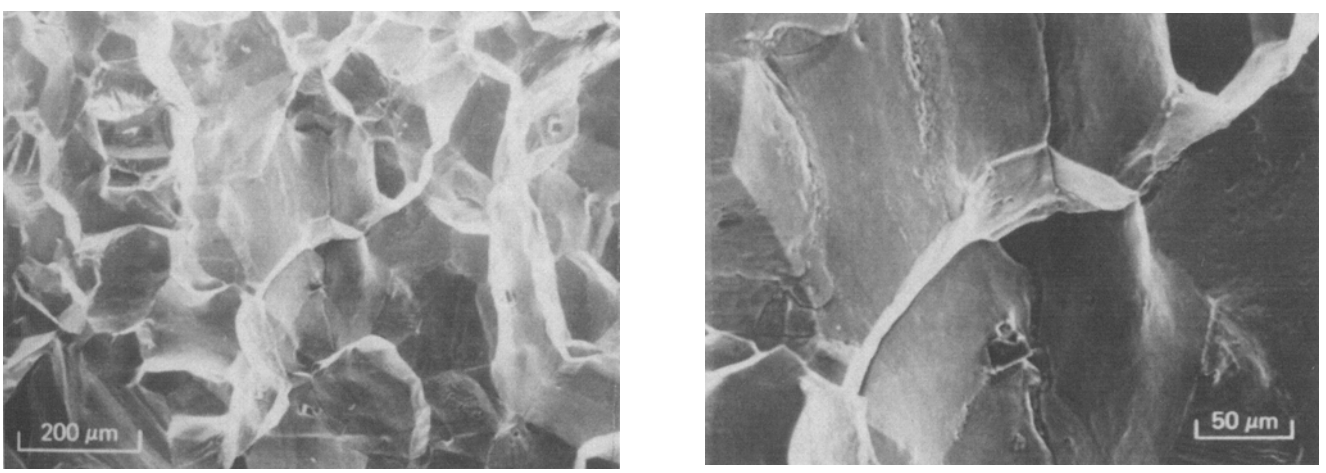


(*c*)

Fig. 4 — Characteristic fracture surfaces of hot ductility samples. (*a*) OH-900 °C, (*b*) OH-1250 °C, (*c*) 1350 °C, and (*d*) OC-1100 °C.

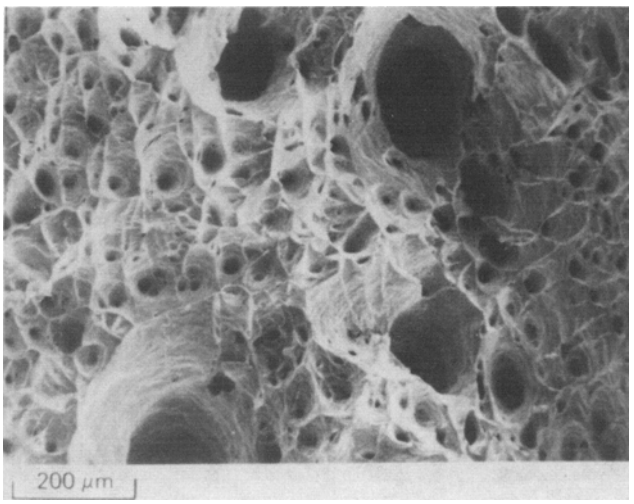


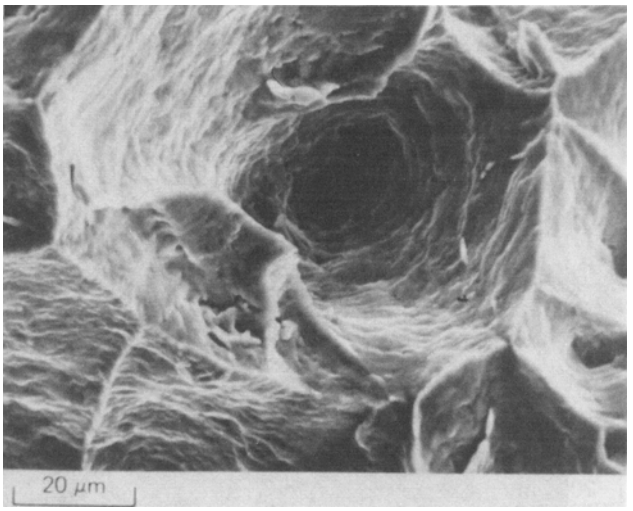


(*d*)

Fig. 4 Cont. — Characteristic fracture surfaces of hot ductility samples. (*a*) OH-900 °C, (*b*) OH-1250 °C, (*c*) 1350 °C, and (*d*) OC-1100 °C.

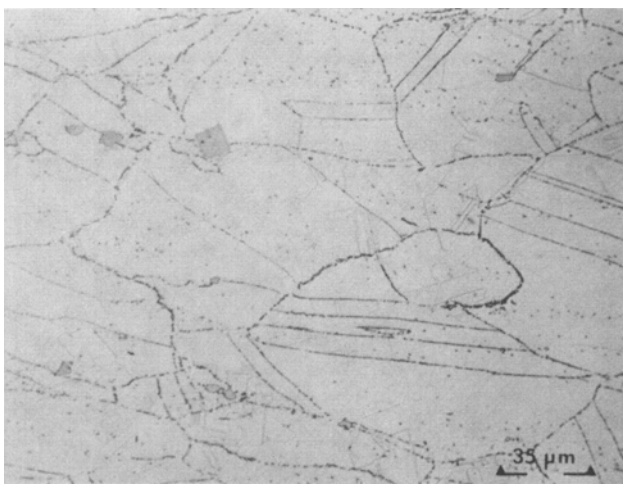


(*a*)

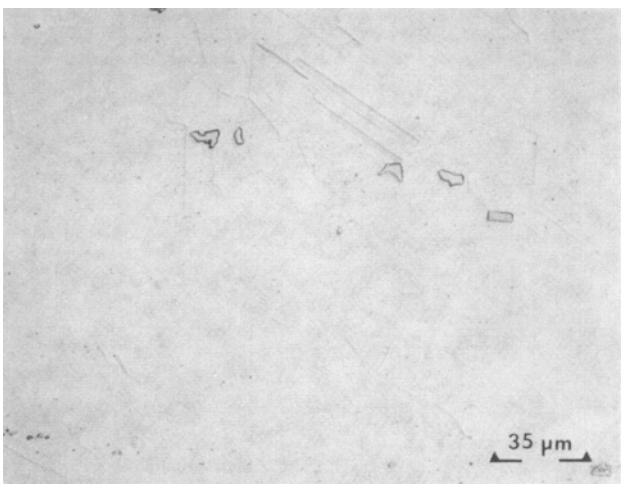


(*b*)

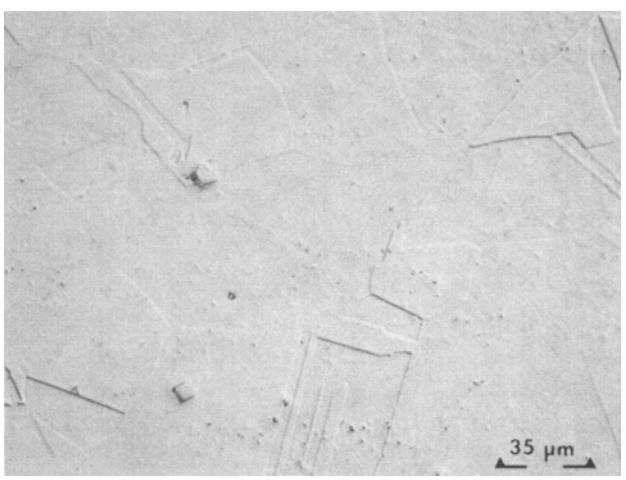


(*c*)

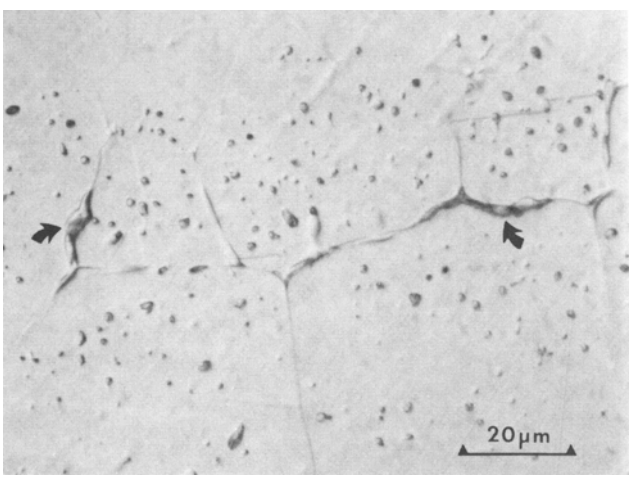


(*d*)

Fig. 5 — Optical micrographs of quenched samples. (*a*) OH-1100 °C, (*b*) OH-1250 °C, (*c*) 1350 °C, and (*d*) OC-1325 °C.

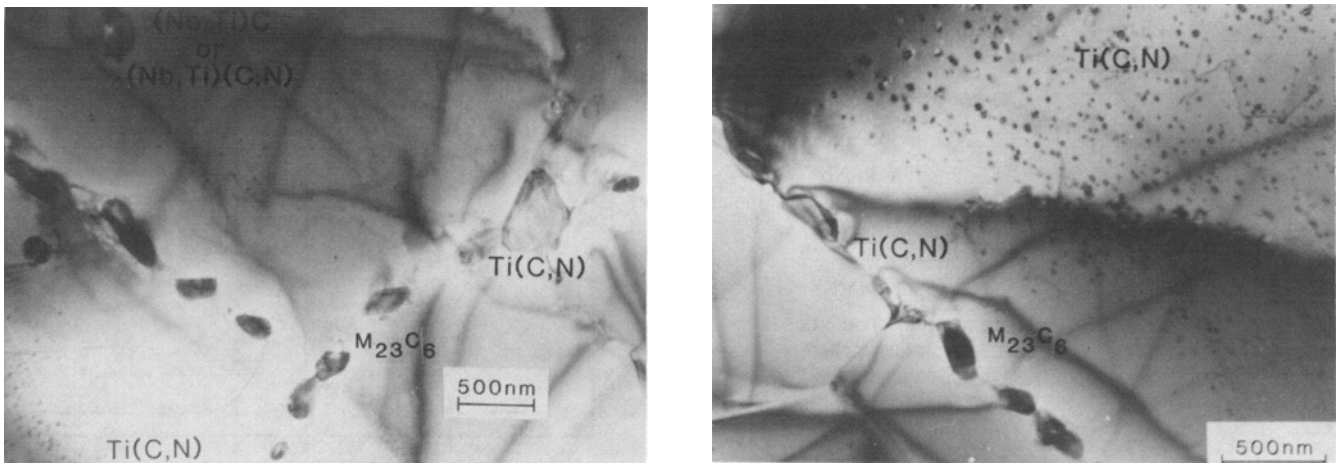


(*a*) (*b*)

Fig. 6 — (*a*) and (*b*) TEM bright-field images of the starting base material. The strain fields due to fine, coherent Ti(C, N) precipitates are shown in the matrix. Matrix (Nb, Ti)C and (Nb, Ti) (C, N) are visible. Grain boundary $M_{23}C_6$ (Cr-rich) and Ti(C, N) are also shown.

have formed in the melt, but their morphology, size, and distribution suggest that they formed through a solid-state reaction during subsequent heat treatment.

The matrix also contained a large, uniformly distributed population of coherent Ti(C, N) carbonitrides (Figure 6(b)). These small precipitates formed through a solid-state reaction, probably during the mill-annealing treatment. These precipitates occurred uniformly throughout the matrix; there was no grain boundary denuded zone. The diameter of the coherent Ti(C, N) was approximately 20 to 30 nm. The Ti(C, N) has the fcc structure with a lattice parameter of 0.428 nm. The measured value is consistent with the reported lattice parameter of 0.421 nm for Ti(C, N).[29] X-ray microanalysis of the larger (30 nm) Ti(C, N) precipitates, in extremely thin regions of the foil (<20 nm thick), showed Ti to be the only metallic species present in the carbonitrides. For the geometrical configuration of interest here, and an 18 nm diameter (Gaussian) probe, Monte Carlo modeling indicates the detectability for Nb to be approximately 1 wt pct. Hence, the carbonitrides are essentially Ti(C, N), not (Ti, Nb)(C, N).[30] The absence of Nb in the carbonitrides is consistent with the lattice parameter measured for this precipitate. The fcc lattice parameter of NbC is 0.447 nm,[29] substantially larger than the measured value of 0.423 nm. The coherent Ti(C, N) exhibited a cube/cube relationship with the austenite. All of the present results on the morphology, distribution, and crystallography of the Ti(C, N) in the austenitic matrix are consistent with the observations of Nahm and Moteff.[31]

The grain interiors also contained large, cuboidal-shaped TiN which are clearly visible in the optical micrograph shown in Figure 1. The TiN are large and widely dispersed; none happens to be present in the TEM micrograph shown in Figure 6. The edge lengths of the TiN precipitates were approximately 6 to 10 $\mu$m. No carbon was detectable in these particles with EPMA. There was no orientation relationship with the matrix, which is consistent with these precipitates being formed initially from the melt.

The grain boundaries of the mill-annealed material were decorated with both irregularly shaped Ti(C, N) and $M_{23}C_6$ precipitates. These precipitates were up to 500 nm in length and 100 nm in width. These Ti(C, N) did contain a trace of Nb, the concentration ratio (from Eq. [1]) of Ti/Nb being approximately 20/1. The $M_{23}C_6$ carbides were Cr-rich, but did contain a small amount of Fe. Once again, Monte Carlo results suggest that the observed level of Fe is greater than that which one would expect if all of the measured Fe was due to fluorescence of Fe in the matrix. Deconvolution of the EDS spectra by Monte Carlo techniques suggests that the Cr/Fe concentration ratio (from Eq. [1]) in the $M_{23}C_6$ carbides is approximately 8/1. The orientation relationships between the grain boundary $M_{23}C_6$ and the grain boundary Ti(C, N) and the parent austenitic matrix were also cube/cube.

It is important to keep the identity and location of the various carbides and carbonitrides in proper perspective when developing the mechanistic model for grain boundary liquation. Table I lists the precipitates present in the initial mill-annealed material. Other important considerations for each type of precipitate are also given.

2. *On-heating microstructures*

Samples quenched from 900 °C and 1100 °C showed no significant microstructural changes relative to the mill-annealed microstructure. A TEM micrograph of a representative region from a sample quenched on-heating from 1100 °C is shown in Figure 7. The structure is highly dislocated, probably as a result of the rapid quench. Note that both the intergranular $M_{23}C_6$ precipitates and the MC-type precipitates are still present in the structure. The fine intragranular Ti(C, N) shown in Figure 6 was also still present in the samples quenched from 900 °C and 1100 °C. The Ti(C, N) are not evident in Figure 7 since the specimen was tilted at an angle relative to the incident electron beam for which the strain fields for the Ti(C, N) are not in contrast.

AEM X-ray microanalysis of clean grain boundaries, as well as those adjacent to the Ti(C, N) and $M_{23}C_6$ precipitates, showed no enrichment of Ti, or any other component, relative to the matrix. The Ti level in the matrix is below the detectability limit of Ti in Fe-Ni-Cr (approximately 0.5 wt pct). This observation is consistent with the bulk

**Table I. Summary of Carbides and Carbonitrides Present in This Heat of Mill-Annealed Alloy 800**

| Precipitate | Location | Comment |
|---|---|---|
| (Nb, Ti)C | intragranular | 1. very rich in Nb<br>2. 200 to 500 nm in diameter |
| (Nb, Ti) (C, N) | intragranular | 1. very rich in Nb<br>2. 200 to 500 nm in diameter |
| Ti(C, N) | intragranular | 1. very small, 20 to 30 nm<br>2. coherent with matrix contained no Nb |
| Ti(C, N) | intergranular | 1. at grain boundaries<br>2. much larger than coherent matrix Ti(C, N)<br>3. 500 nm long, 100 nm wide contained a trace of Nb Ti/Nb ~ 20/1 |
| TiN | intragranular | 1. very large, 6 to 10 $\mu$m<br>2. from original melt |
| $M_{23}C_6$ | intragranular | 1. Cr-rich Cr/Fe ~ 8/1<br>2. 500 nm long, 100 nm wide |

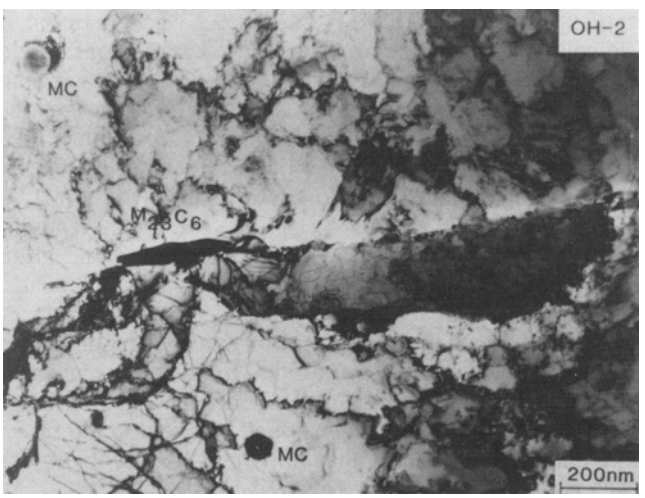


Fig. 7—TEM bright-field image of on-heating sample quenched from 1100 °C. The microstructure is essentially unchanged from the starting microstructure with the exception of the heavy dislocation substructure.

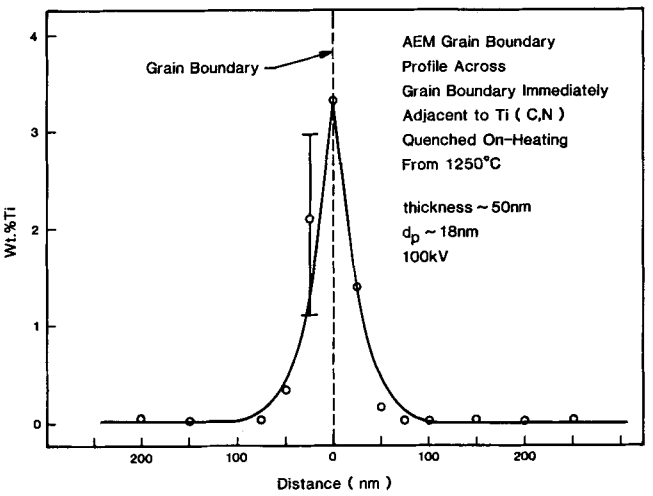


(*a*)

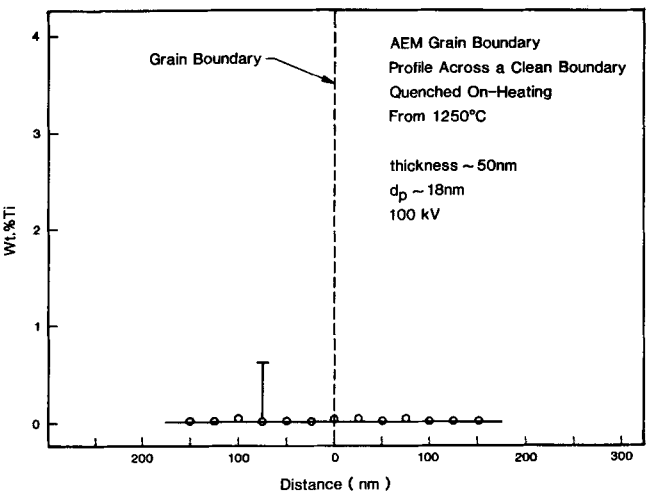


(*b*)

Fig. 8—(*a*) Concentration profile, measured by AEM X-ray microanalysis, across a grain boundary immediately adjacent to a Ti(C, N) precipitate in the 1250 °C on-heating sample. The profile was measured 50 to 100 nm from the Ti(C, N) to prevent fluorescing of Ti from the precipitate. Evidence suggests that the enrichment occurred due to solid state dissolution of the Ti(C, N) and subsequent diffusion of Ti down the grain boundary. (*b*) Concentration profile taken across a clean grain boundary in the 1250 °C on-heating sample. The concentration of Ti is below the detectability limit for AEM microanalysis in the matrix and at the grain boundary.

alloy chemistry (0.49 wt pct Ti) and the fact that the Ti level in the matrix is considerably smaller than the bulk Ti level since much of the Ti has been depleted from the matrix to form the various carbides and carbonitrides observed in the alloy. These data indicate that the Ti(C, N) solvus is not exceeded at temperatures up to 1100 °C.

The microstructure of the on-heating sample quenched from 1250 °C appeared essentially like the mill-annealed specimen except for the first indication of grain growth, which is consistent with the subtle variation shown by optical metallography in Figure 5(b). However, the 1250 °C on-heating sample was the first to show any signs of Ti enrichment at the grain boundaries. Figure 8(a) shows a concentration profile, measured by AEM X-ray microanalysis, across a grain boundary immediately adjacent to a Ti(C, N) precipitate. The profile was measured 50 to 100 nm away from the Ti(C, N) to avoid fluorescing any Ti from the Ti(C, N). The measured peak concentration of Ti is approximately 3.3 wt pct. The X-ray generation volume is most likely larger than the Ti enriched layer, so the 3.3 wt pct may actually be an average of the boundary-enriched layer and the matrix. Without knowing the exact width of the Ti-enriched layer, it is impossible to determine the composition of the enriched layer explicitly. Figure 8(b) shows a similar concentration profile measured at a clean grain boundary, totally void of Ti(C, N). No enrichment of Ti, within the detectability limit of AEM X-ray microanalysis, is present. No other elemental enrichment at the grain boundaries was observed in the on-heating 1250 °C sample.

The sample quenched from 1300 °C exhibited more pronounced signs of grain growth than the on-heating samples quenched from lower temperatures. However, grain growth is not yet complete. As shown in Figure 9(a), $M_{23}C_6$ precipitates are still stable along grain boundaries at this temperature. In addition, the fine, coherent Ti(C, N) remains relatively unchanged in both distribution and morphology (Figure 9(b)) from the starting microstructure.

There was also enrichment of the grain boundaries immediately adjacent to the grain boundary Ti(C, N) in the on-heating sample quenched from 1300 °C, as shown in Figure 10(a). Once again, as shown in Figure 10(b), the clean grain boundaries showed no enrichment. The level of enrichment is significantly higher, approximately 13.0 wt pct Ti, than observed in the 1250 °C on-heating sample. As will be described in more detail later, these results may suggest that the enrichment at 1250 °C is due to solid state dissolution of the Ti(C, N) and diffusion of Ti down the grain boundary, while the enrichment at 1300 °C is due to the first formation of a liquid film which has wetted the grain boundary. No other elemental enrichment at the grain boundaries was observed in the on-heating 1300 °C sample.

At the peak temperature, 1350 °C, grain growth is extensive and carbide and carbonitride dissolution is evident.

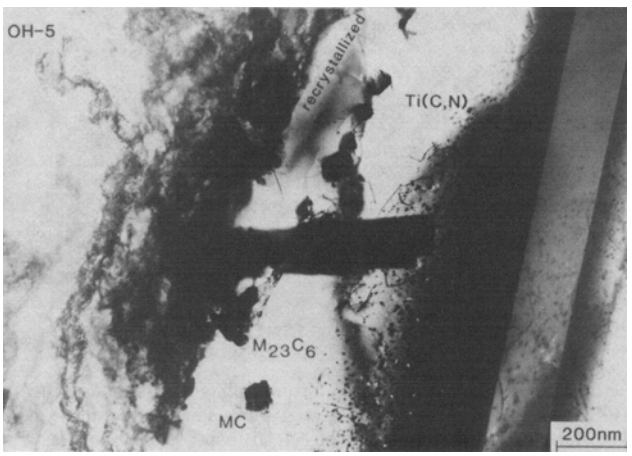


(*a*)

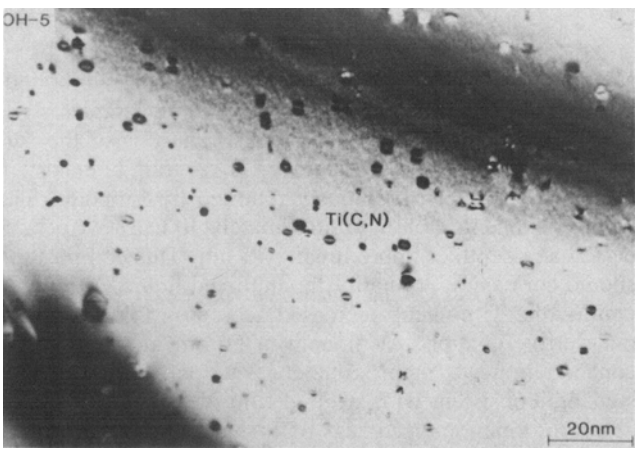


(*b*)

Fig. 9 — TEM bright-field image of on-heating sample quenched from 1300 °C. Note: (*a*) evidence of recrystallization and retention of $M_{23}C_6$ along grain boundaries and (*b*) coherent Ti(C, N) and strain doublets associated with these precipitates.

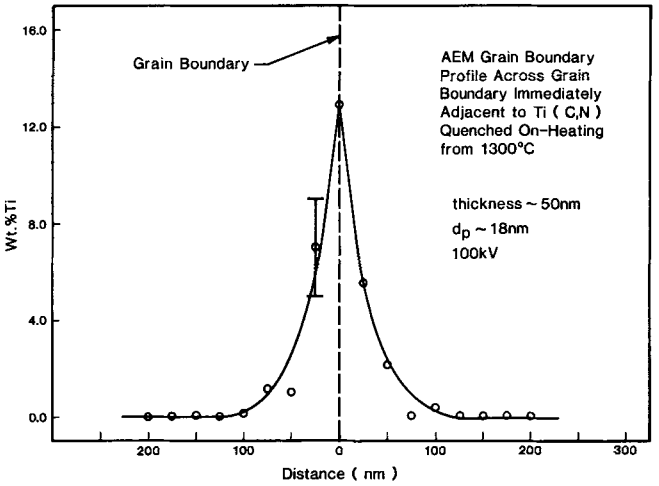


(*a*)

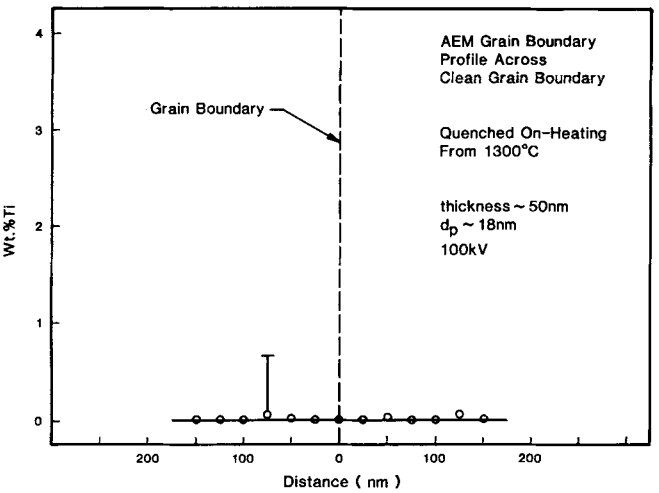


(*b*)

Fig. 10 — (*a*) Concentration profile, measured by AEM X-ray microanalysis, across a grain boundary immediately adjacent to a Ti(C, N) precipitate in the 1300 °C on-heating sample. The profile was measured over 50 nm from the Ti(C, N) to prevent fluorescing of Ti from the precipitate. Evidence suggests that the enriched layer was formed by the intrusion of a liquid film. (*b*) Concentration profile taken across a clean grain boundary in the 1300 °C on-heating sample. The concentration of Ti is below the detectability limit for AEM microanalysis in the matrix and at the grain boundary.

Most, if not all, of the fine intergranular Ti(C, N) has dissolved and dissolution of the $M_{23}C_6$ grain boundary precipitates has commenced. The larger matrix (Nb, Ti)C and (Nb, Ti) (C, N) appear to be thermodynamically stable at these temperatures and no dissolution was observed. A representative TEM micrograph of this structure is shown in Figure 11. Liquation of Ti(C, N) is still not apparent. However, one must appreciate that the early stages of liquation and first wetting of the grain boundaries may not be observable by conventional TEM.

3. *On-cooling microstructures*

All samples quenched on-cooling from 1350 °C exhibited a microstructure which was completely recrystallized and had undergone substantial grain growth. Heating through the peak temperature allowed nearly complete dissolution of the fine, coherent Ti(C, N) and the grain boundary $M_{23}C_6$.

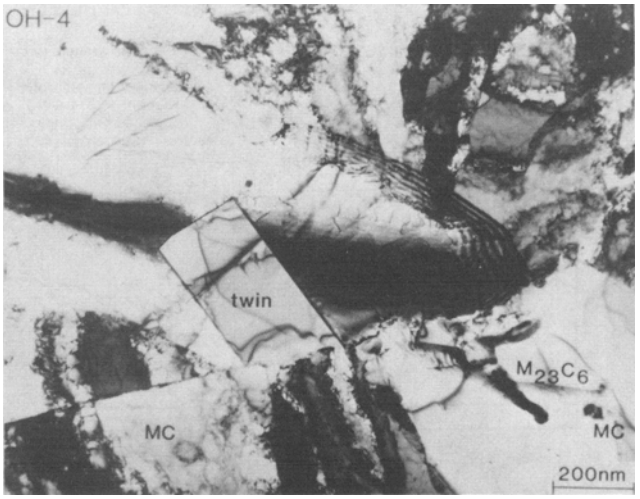


Fig. 11 — TEM bright-field image of the on-heating sample quenched from 1350 °C. Recrystallization is extensive and the fine, coherent Ti(C, N) has dissolved. Larger $M_{23}C_6$ precipitates are still present along the grain boundaries.

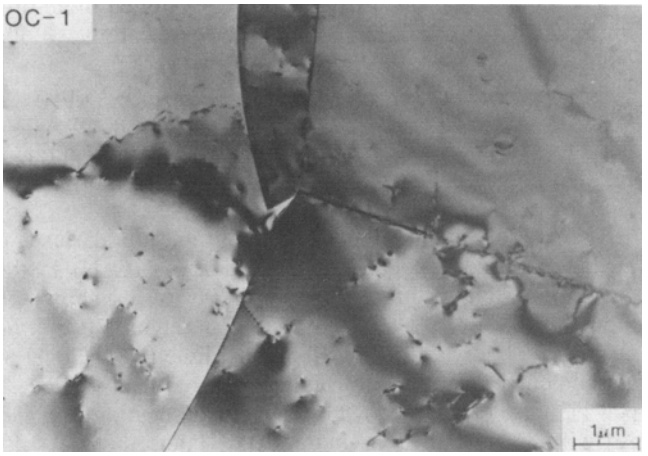


Fig. 12 — TEM bright-field image of on-cooling sample quenched from 1325 °C. The recrystallized microstructure is shown with retained (Nb, Ti)C or (Nb, Ti) (C, N).

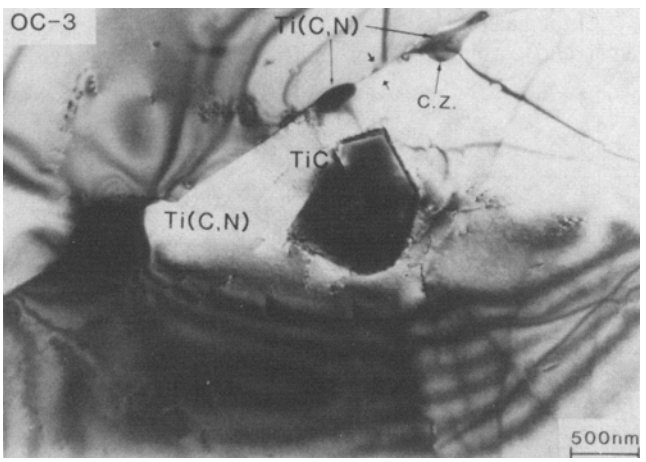


Fig. 13 — TEM bright-field image of on-cooling sample quenched from 1100 °C. Evidence of liquation is seen surrounding the grain boundary Ti(C, N). The liquation produces the "cloudy zone" at the grain boundary. Position of concentration profile, shown in Fig. 12(a), taken across grain boundary is indicated by arrows.

A TEM micrograph of the representative structure from a sample quenched at 1325 °C is shown in Figure 12. The only features present in this micrograph are a few grain boundaries, twin boundaries, and a sparse dislocation substructure. The original (Nb, Ti)C and (Nb, Ti) (C, N) still remain, although none is shown in Figure 12.

All the grain boundary Ti(C, N) present in the on-cooling samples were irregular in shape and were surrounded by "cloudy zones." An example of this zone is shown in Figure 13 from an on-cooling sample quenched from 1100 °C. The "cloudy zone" is the first visual indication of liquation which occurs during the simulated HAZ thermal cycle. The "cloudy zone" corresponds to extensive constitutional liquation of the Ti(C, N). EDS analysis revealed that the "cloudy zones" are enriched in Ti relative to the surrounding matrix. The measured Ti content varied from approximately 10 to 13 wt pct Ti in the resolidified Fe-Ni-Cr austenite. The Ti content of the residual Ti(C, N) found at the core of some of the "cloudy zones" contained almost 80 wt pct Ti. The measured ratios of Ni/Fe and Cr/Fe in the "cloudy zones" were approximately 0.7 and 0.4, respectively, which is consistent with the same elemental ratios in the bulk alloy. The wide variation in Ti content is due to mixing effects, *i.e.*, how much of the surrounding Fe-Ni-Cr matrix has mixed with the Ti released by the liquating Ti(C, N). The "cloudy zones" do not have internal structure, which suggests that the liquid Ti-Fe-Ni-Cr solidified epitaxially from the adjacent solid matrix. There was no evidence of carbides, nitrides, or carbonitrides in or near the "cloudy zones," which suggests that the C and N diffused into the matrix upon liquation and were therefore not present during resolidification. The grain boundaries immediately adjacent to the "cloudy zones" also showed Ti enrichment. A composition profile taken across the boundary between the two "cloudy zones" shown in Figure 13 is given in Figure 14(a). The apparent level of Ti at this grain boundary is approximately 13.9 wt pct. The level of enrichment observed in the 1100 °C on-cooling sample is statistically identical to the enrichment observed in the 1300 °C on-heating sample. No other elemental enrichment at the grain boundaries was observed in any of the on-cooling samples.

Auger electron spectroscopy (AES) analysis of the surface present at the site of a liquated HAZ grain boundary in Alloy 800 has been previously reported by Lippold.[4] The peak Ti concentration of approximately 10 to 18 wt pct occurred at a depth of approximately 5 nm. This composition should correspond to that of the unmixed liquid. At greater depths, the Ti content decreased according to an approximate error function. At a depth of 50 nm, the residual Ti concentration was approximately 3 wt pct. The AEM results are consistent with a liquid film of these dimensions. The error function type decay of Ti in the matrix adjacent to the liquid is consistent with a Ti profile one would expect due to the diffusion of Ti into austenite in the solid state at a temperature of 1300 °C over a time interval of a few seconds.[32,33] If the Ti diffusion occurred in an unmixed liquid, the interdiffusion distance would be much greater.

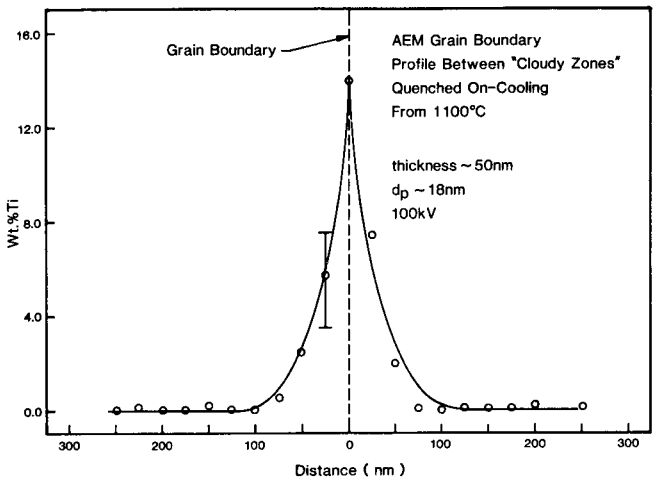


(*a*)

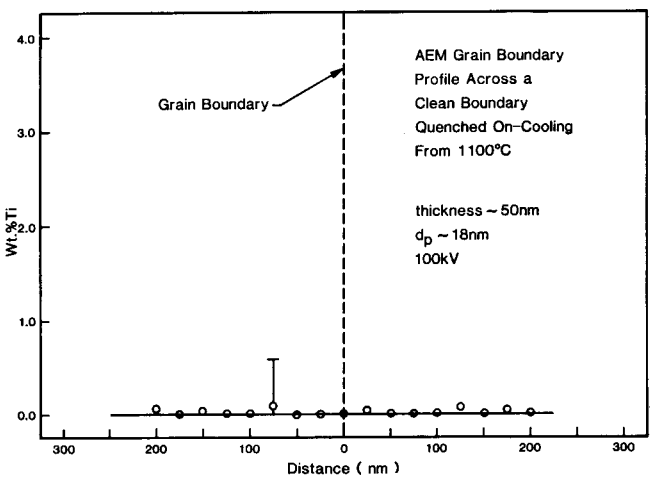


(*b*)

Fig. 14—(*a*) Concentration profile, measured by AEM X-ray microanalysis, taken across grain boundary near liquating Ti(C, N) in on-cooling sample quenched from 1100 °C. Position of profile indicated by arrows in Fig. 13. (*b*) Concentration profile taken across clean grain boundary in on-cooling sample quenched from 1100 °C. The concentration of Ti is below the detectability limit for AEM X-ray microanalysis in the matrix and the grain boundary.

The quantitative consistency between the AES and AEM results is explicitly shown in the Appendix.

Grain boundaries which were not associated with Ti(C, N) precipitates and the surrounding "cloudy zones" showed no evidence of Ti enrichment. The absence of Ti enrichment at clean grain boundaries, such as those shown in Figure 10(b), is apparent in the composition profile measured across a clean grain boundary in a sample quenched from 1100 °C on-cooling as shown in Figure 14(b). Intermetallic phases, such as $Fe_2Ti$ or $(Fe, Ni)_2Ti$ (Laves), were not observed in any of the samples.

The coherent matrix Ti(C, N) was not present in any of the on-cooling samples. On passing through the peak temperature all of the Ti(C, N) dissolved. There was insufficient time at temperature for the Ti(C, N) to reprecipitate on cooling, which is consistent with earlier kinetic observations in Alloy 800.[21]

## IV. DISCUSSION

### A. *The Measurement of Boundary Compositions by AEM*

The observations made by optical metallography, elemental mapping by electron microprobe, imaging and electron diffraction by conventional transmission electron microscopy, and X-ray microanalysis by analytical electron microscopy all suggest that the observed grain boundary melting is due to a constitutional liquation driven eutectic-type reaction between the grain boundary Ti(C, N) and the austenitic matrix. The critical observation which leads one to this conclusion is the Ti enrichment of the grain boundaries adjacent to the "cloudy zones" associated with the dissolving grain boundary Ti(C, N) and the absence of Ti enrichment at grain boundaries not associated with the Ti(C, N). The lack of general enrichment of Ti at all grain boundaries, except in the vicinity of grain boundary Ti(C, N), at temperatures in excess of 1250 °C, argues against the Ti enrichment at grain boundaries *via* an equilibrium volume diffusion process or a grain boundary sweeper mechanism. Since Ti enrichment at the liquating boundaries is paramount to the proposed hot-cracking mechanism, it may be useful to consider in detail the detection of grain boundary films by AEM X-ray microanalysis. For a more detailed description of the AEM techniques used to quantify the level of Ti enrichment at the grain boundaries in the current study, the reader is referred to the Appendix.

### B. *Proposed Phase Transformation Mechanism*

The proposed phase transformation mechanism must be consistent with all experimental observations which describe the grain boundary liquation and subsequent hot-cracking. Furthermore, the model must be consistent with any previous data on the transformation behavior of Alloy 800.

It is critical to recognize that transformations which occur in the heat-affected zone of an actual weld or in a Gleeble sample may not represent thermodynamic equilibrium. The heating and cooling rates are so rapid that in most cases there is insufficient time to establish equilibrium. Hence, given sufficient time, some of the transformations observed in the current study may occur at lower temperatures.

#### 1. *Constitutional liquation*

On-heating, the original mill-annealed microstructure, is stable until approximately 1250 °C. At this point grain growth begins. Dissolution of the carbides and carbonitrides is not yet apparent, even in the TEM micrographs. However, the Ti enrichment along grain boundaries adjacent to Ti(C, N) in the 1250 °C on-heating sample suggests that some dissolution of the Ti(C, N) has commenced. The observed level of Ti enrichment, 3.3 wt pct Ti, with respect to Eq. [A-6] (Appendix), could suggest an enriched film of the liquid composition (14 wt pct Ti) approximately 8 nm thick. However, the high ductility observed in the 1250 °C on-heating sample indicates that liquation has not yet begun. However, solid state diffusion of Ti along the grain boundary could also produce the observed enrichment. From Eq. [A-6] (Appendix), a 100 pct Ti film, approximately 1.5 nm thick, would produce the observed apparent concentration. A 1 to 2 nm thick film is consistent with grain boundary dimensions.[18] These results would suggest that the

solvus for dissolution of grain boundary Ti(C, N), with its unique C/N ratio, in austenite of this composition, is less than 1250 °C. One might also expect the dissolution of the coherent Ti(C, N) to commence. However, the grain boundary Ti(C, N) does contain a trace of Nb (wt pct ratio of Ti/Nb is approximately 20/1) and the C/N ratio for the coherent Ti(C, N) and the grain boundary Ti(C, N) may be different, which could result in different solvus temperatures.

At 1300 °C, the reduction in area is decreased by ~50 pct from that observed at 1250 °C. This loss of ductility can be attributed to either a continuing increase of the amount of intergranular *vs* ductile failure as the equicohesive temperature is exceeded or the initiation of grain boundary liquation. There is evidence which supports both hypotheses. The failure loads do not drop precipitously as the ductility falls, suggesting that total liquation is not occurring. Rather, a solid state grain boundary fracture is suggested. Simultaneously, though, the observed level of grain boundary Ti enrichment adjacent to the Ti(C, N) is consistent with the AEM and AES results of specimens known to have undergone liquation. This may be indicative of localized liquation in the vicinity of the grain boundary Ti(C, N) only. Either mechanism would act to reduce ductility.

On heating through the peak temperature, 1350 °C, the small, coherent matrix Ti(C, N) and grain boundary $M_{23}C_6$ dissolve. The extensive liquation of the grain boundary Ti(C, N) gives rise to the "cloudy zones." The equilibrium dissolution temperature for these precipitates may be lower, but there was insufficient time at lower temperatures to permit dissolution. When these precipitates dissolve, the Ti, Cr, C, or N go into solution in the austenitic matrix. These components stay in solution. There is no thermodynamic driving force to move these elements to the grain boundaries; the levels released into solution in the matrix are well below the solubility limit in austenitic Fe at this temperature.[34] The liquid which forms initially contains Fe, Ni, Cr, Ti, C, and N. The high level of C and N in the liquid relative to the matrix creates a potential gradient which causes the C and N to diffuse into the surrounding matrix. The diffusion rate of Ti in austenite is too sluggish to allow it to diffuse deeply into the surrounding matrix. The diffusivity of Ti, C, and N in austenite at 1300 °C are estimated to be $1.5 \times 10^{-8}$ cm$^2$/sec, $4.2 \times 10^{-6}$ cm$^2$/sec, and $1.0 \times 10^{-4}$ cm$^2$/sec, respectively.[32] Solving the diffusion equation for diffusion from a plane source,[33] in one second, the Ti could diffuse only 1.5 $\mu$m, while C and N could diffuse 30 and 120 $\mu$m, respectively. Even if the total time were 10 seconds, the Ti could diffuse only 6 $\mu$m, which is much less than the average grain size. Hence, the liquid quickly becomes Ti-Fe-Ni-Cr. When the temperature decreases, the metal resolidifies epitaxially upon the matrix. Since the carbon is now absent, there is no reason to expect a metal/carbide eutectic structure to form. The C and N released into the matrix stay in solution, since there is insufficient time to nucleate new carbides and carbonitrides.[21]

The strongest evidence for liquation due to dissolution of carbides is the formation of the "cloudy zones," as shown in Figure 13. It is postulated, from this TEM evidence, that as the carbides dissolve, the C and N diffuse into the matrix, leaving C and N free metal to later resolidify epitaxially from the austenite. These observations suggest that the dissolution process does not occur at equilibrium. Under equilibrium dissolution, the liquid metal would always contain C and N until the interior Ti(C, N) has completely dissolved. The C and N concentration at the Ti(C, N) interface would be the equilibrium value of C and N saturated liquid, while the liquid/austenite interface C and N concentrations would be some smaller value. Under these equilibrium conditions, when the metal solidifies one would expect a two phase mixture of Ti(C, N) and austenite, rather than single phase epitaxially formed austenite. This suggests that dissolution did not occur at equilibrium and was not controlled by diffusion of C and N through the liquid from the Ti(C, N) to the austenite. Rather, the dissolution process was controlled by interfacial dissolution kinetics between the liquid and the Ti(C, N). Under interface control, diffusion through the liquid would produce low levels of C and N in the liquid so that resolidification would occur as austenite, rather than a Ti(C, N) plus austenite mixture. The Ti content of the liquid is low enough, approximately 10 to 13 wt pct Ti, that resolidification would produce austenite rather than an austenite plus Laves mixture.[34]

The matrix TiC and (Nb, Ti)C and (Nb, Ti)(C, N) do not participate in the liquation reaction. It is likely that either the austenite/TiC, austenite/(Nb, Ti)C, and austenite/(Nb, Ti)(C, N) eutectic temperatures exceed 1350 °C in Alloy 800 or the reaction kinetics are too sluggish to permit liquation.

The hot ductility (Gleeble) results, optical metallography, fractography, and AEM all suggest that grain growth and solid state dissolution of the grain boundary Ti(C, N) begin by 1250 °C and localized liquation reaction begins by 1300 °C. The question here is what components are involved in the liquation reaction. It is proposed that a non-equilibrium constitutional liquation driven eutectic-type reaction between the austenitic matrix and the grain boundary Ti(C, N) occurs. Similar matrix/carbide eutectic-type liquation reactions have been reported in other stainless steels by Pepe and Savage[6] and in Ni alloys by Savage and Krantz.[7]

At 1300 °C, there is evidence of the initiation of liquation of the Ti(C, N). In specimens not subjected to a fracture load (water quenched specimens from which the thin foils were obtained), the liquid wets the grain boundaries adjacent to the liquating Ti(C, N). Grain boundary wetting would be enhanced under an applied stress, where induced capillary action would spread the liquid along grain boundaries.[35,36] The relatively high level of failure stress at all temperatures below the zero strength temperature (both on heating and cooling) suggests that complete grain boundary wetting due solely to the liquation of Ti(C, N) does not occur. Rather, it is likely that localized melting occurs and the contribution of this melting to failure (either in a simulated or real HAZ) would be dependent on the application of stress to extend this liquid along grain boundaries. Based upon these observations, it can be concluded that the extent of expected HAZ hot cracking would not be great in this alloy.

2. *Consistency with previous studies*

Fe-Ti and Ni-Ti or (Fe, Ni)-Ti intermetallic compounds (Laves phase) have not been observed in any Alloy 800 hot ductility sample. This is consistent with the work of Adamson *et al.*,[14] in that alloys containing less than 1 wt pct Ti did not form Laves phase even after a 1-hour heat treatment at 1350 °C. Laves phase, however, has been

observed in the HAZ of alloy A-286,[11] where it formed as the decomposition product of Mo-enriched TiC or Ti(C, N). It is likely that the relatively large concentration of Laves-forming elements (Ti, Mo, Si) in the A-286 studied previously[11] allowed for the formation of this constituent. Interestingly, it was observed in the study of A-286 HAZ cracking susceptibility[11] that cracking was eliminated when Ti and Si concentrations were reduced from nominal concentrations (from 2.2 to 1.6 wt pct for Ti and 0.6 to 0.16 wt pct for Si), suggesting a reduction or elimination of the Laves phase. The paper was not specific on this issue.[11] Clearly, the formation of the Laves intermetallic constituent in alloys of this general Fe and Ni concentration is both dependent on specific composition and thermal history.

3. *Thermodynamic consequences*

Since forming the austenitic solid solution represents the state of lowest free energy, Ti will not in general segregate to the grain boundaries.[37,38] The limitation preventing Ti segregation to the grain boundaries is therefore thermodynamic, not kinetic (volume diffusion). If the limitation were kinetic, then the movement of grain boundaries through the matrix would facilitate segregation to the grain boundaries. More rapid segregation of an impurity to a grain boundary due to the movement of the grain boundaries through the supersaturated matrix gives rise to the so-called sweeper mechanism. If a grain boundary sweeper mechanism, sweeping Ti to the prior grain boundaries, were active, most, if not all, grain boundaries would be Ti enriched. Consequently, there is no evidence to support a grain boundary sweeper mechanism in this case.

4. *Summary*

The liquation reaction proposed for the Alloy 800 examined in this study is similar to the matrix/carbide (carbonitride) reaction observed by earlier investigators.[11,14] The phase transformation sequence is summarized in Table II. In the present study, there was either insufficient time or insufficient Ti to nucleate the intermetallic phases that were observed by earlier investigators.[11,14] Regardless, the operative mechanism for subsolidus grain boundary liquation in this heat of Alloy 800 is consistent with constitutional liquation of Ti(C, N). The results of hot ductility testing can be used to suggest that the extent of HAZ hot cracking expected in this alloy would be slight as the reduction in area data during both the on-heating and on-cooling portions of the thermal cycle are similar (offset by only ~25 °C) and a substantial fracture stress is required even when the specimens exhibit low ductilities.

**Table II. Proposed Phase Transformation Sequence Leading to HAZ Grain Boundary Liquation in On-Heating in Alloy 800**

| Temperature | Phase Reaction |
|---|---|
| <1250 °C | 1. mill-annealed structure is stable |
| ~1250 °C | 1. grain growth begins<br>2. solid-state dissolution of grain boundary Ti(C, N) commences<br>3. grain boundary diffusion leads to local enrichment of boundaries near Ti(C, N) with Ti |
| 1250 to 1300 °C | 1. liquation of grain boundary Ti(C, N) commences (coincident with dramatic loss in ductility) (liquid wets grain boundaries near liquating carbonitrides)<br>2. all other carbides and carbonitrides remain stable |
| 1300 to 1350 °C | 1. liquation of grain boundary Ti(C, N) is extensive leading to formation of "cloudy zones" (more extensive wetting of grain boundaries)<br>2. coherent matrix Ti(C, N) dissolves<br>3. grain boundary $M_{23}C_6$ dissolves<br>4. Nb-rich carbides and carbonitrides remain stable |

## V. CONCLUSIONS

1. The observed grain boundary liquation in simulated HAZ specimens in this heat of mill-annealed Alloy 800 is consistent with a constitutional liquation driven non-equilibrium eutectic-type reaction between the austenitic matrix and the grain boundary Ti(C, N).
2. The solvus temperature for grain boundary Ti(C, N) found in this heat of Alloy 800 is less than 1250 °C.
3. HAZ grain boundary liquation in Alloy 800 begins by 1300 °C. This result is supported by hot ductility (Gleeble) data, optical metallography, fractography, and analytical electron microscopy.
4. Only the grain boundaries adjacent to Ti(C, N) show Ti enrichment. At 1250 °C, the enrichment is due to the solid state dissolution of the Ti(C, N) and subsequent Ti diffusion down the grain boundary. At temperatures greater than 1300 °C, the enrichment is due to the liquation of the Ti(C, N) and subsequent wetting of the adjacent grain boundaries. Grain boundaries which did not contain Ti(C, N) did not show any Ti enrichment.
5. Resolidification of the Ti-enriched grain boundary liquid occurs by epitaxial growth on the austenitic matrix. The carbonitride structure is not evident as the free C and N produced in the liquation reaction diffuse readily down a concentration gradient into the bulk matrix.
6. No evidence was found for the formation of either $Fe_2Ti$ or $Fe_2Nb$ Laves phases along the liquated grain boundaries. Relative to previous studies,[11,14] it can be concluded that either the kinetics of formation of these intermetallic compounds is too sluggish during this thermal cycle or the Ti content of the alloy is too low to allow for the formation of these intermetallic phases.
7. There is no evidence for Ti enrichment at grain boundaries due to volume diffusion or a grain boundary sweeper mechanism.
8. Gleeble test results suggest that this heat of Alloy 800 would not be highly susceptible to HAZ cracking.
9. The AEM is a viable technique for examining elemental segregation to grain boundaries in weld HAZ's. The results obtained by AEM are consistent with those obtained by AES.

## APPENDIX

A simple, yet realistic approach for evaluating the composition of grain boundary films by AEM X-ray microanalysis was developed to evaluate the segregation of Bi to grain boundaries in Cu.[14] This model uses the volume ratio of the grain boundary region to the entire volume of X-ray generation to determine the enrichment at the grain boundaries. In the current work, a modified version of this model was used to evaluate the enrichment of Ti at the grain boundaries in Alloy 800.

Broadening of the beam, due to elastic scattering of the electrons, requires that the incident beam sample both the matrix and the grain boundary enriched region simultaneously. Consequently, the measured concentration of Ti is actually the average Ti content of the X-ray generation volume. The true Ti concentration at the grain boundary will be much larger. To evaluate the true Ti concentration at the grain boundary, a mathematical description of the X-ray generation volume is required. Since the total electron path length through a thin foil is short and the incident electrons are very high in energy, the X-ray generation volume and the electron scattering volume are equal. The simplest approach to the interaction volume is to assume an incident beam of diameter $d_p$ and calculate a beam broadening $b$. The incident electron probe is essentially Gaussian, so the diameter of the electron scattering volume, $B$, can be determined in quadrature as:

$$B = (d_p^2 + b^2)^{1/2} \qquad [A\text{-}1]$$

This approach then treats the interaction volume as the frustum of a cone with small diameter $d_p$ and large diameter $B$, as shown in Figure 15. In this case, the interaction volume contains a grain boundary enriched zone of width $\delta$.

If the foil is thin and the scattering power of the atoms in the foil relatively weak, the beam broadening, $b$, can be determined from a single scattering model as:[26]

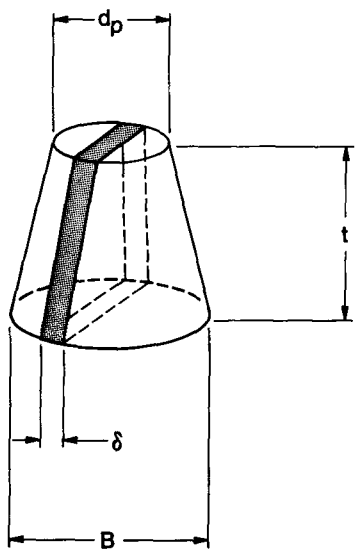


Fig. 15—Schematic representation of electron beam interaction with a grain boundary in a thin slab specimen. In this case, the volume of interaction is modeled as the frustum of a cone. $d_p$ is the incident probe diameter. B is a diameter of the electron beam upon exiting the foil as determined by summing $d_p$ and the beam broadening, $b$, in quadrature.

$$b = 625(Z/E)(p/A)^{1/2}t^{3/2} \quad \text{(cm)} \qquad [A\text{-}2]$$

where $Z$ is the average atomic number, $E$ is the incident beam energy in kV, $p$ is the density in g/cm$^3$, $A$ is the average atomic weight, and $t$ is the foil thickness in cm. Given $d_p$ and $b$, one can calculate $B$ and determine the volume of electron interaction. The total interaction volume is:

$$V_T = \frac{(\pi * t)}{3}(d_p^2 + d_p * B + B^2) \qquad [A\text{-}3]$$

where $t$ is still the foil thickness. The volume of the enriched region included in the interaction volume is:

$$V_{gb} = \frac{\delta t}{2}(d_p + B) \qquad [A\text{-}4]$$

The matrix volume, $V_m$, is simply the difference between the interaction volume, $V_T$, and the grain boundary volume, $V_{gb}$, or:

$$V_m = V_T - V_{gb} \qquad [A\text{-}5]$$

If the grain boundary ($V_{gb}$) and matrix ($V_m$) volumes and the grain boundary ($C_{gb}$) and matrix ($C_m$) compositions are known, the apparent (measured) Ti concentration at the grain boundary, $C_{apr}$, is:

$$C_{apr} = \frac{(V_{gb}C_{gb} + V_mC_m)}{V_T} \qquad [A\text{-}6]$$

Unfortunately, Eq. [A-6] cannot be solved explicitly in this case since both $V_{gb}$ and $C_{gb}$ are unknown. One cannot even reliably estimate $V_{gb}$ since the thickness of the Ti enrichment is unknown. One cannot assume the thickness to be necessarily simply the width of a grain boundary. However, relationships between the width of the Ti-enriched region, the actual average composition of the enriched region, and the apparent composition at the boundary can be calculated. The results of such a calculation are shown in Figure 16. For the current experiments, the incident beam diameter was approximately 18 nm and the thickness of the foil approximately 50 nm.

As stated in the Results, the grain boundary enrichment data obtained by AEM and AES were consistent. Since the spatial resolution of AEM X-ray microanalysis in this case is approximately 30 nm, the AEM would measure the Ti-enriched zone as a layer 50 nm thick (spatial dimension over which concentration decreases to essentially zero by AES analysis) with a nominal composition of 17.5 wt pct. The measured value of $C_{apr}$ was approximately 13.0 wt pct Ti in the 1300 °C on-heating sample and approximately 13.9 wt pct Ti in the 1100 °C on-cooling sample. The agreement between the model prediction and the experimental value is exceptional. The correlation between the AES and AEM X-ray microanalysis results is indicated by the circle shown on Figure 16. The circle represents the Ti-enriched layer composition averaged over a thickness of 50 nm.

The difficulty with AEM X-ray microanalysis is that if the enriched layer thickness is less than the spatial resolution of the analysis, unique values of the enriched layer thickness and enriched layer composition cannot be determined. One can, however, calculate combinations of enriched layer thickness and enriched layer composition which yield the measured apparent enrichment under a specified set of experimental conditions. The results of such a calculation

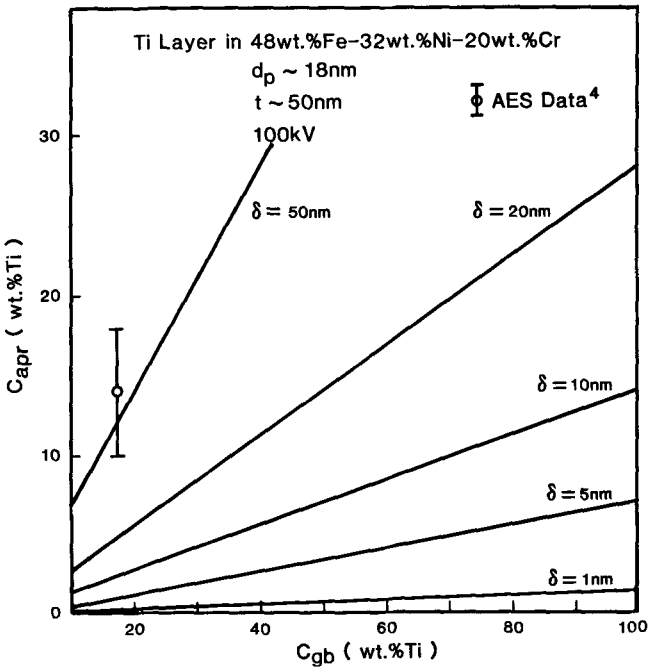


Fig. 16—Results of a calculation which show the relationship between the actual grain boundary enrichment of Ti in austenite and the apparent enrichment of Ti, as measured by AEM X-ray microanalysis, as a function of the width of the enriched layer, *w*. The circle indicates the results of AES, which is in exceptional agreement with the grain boundary enrichment measured by AEM and shown in Fig. 14(b).

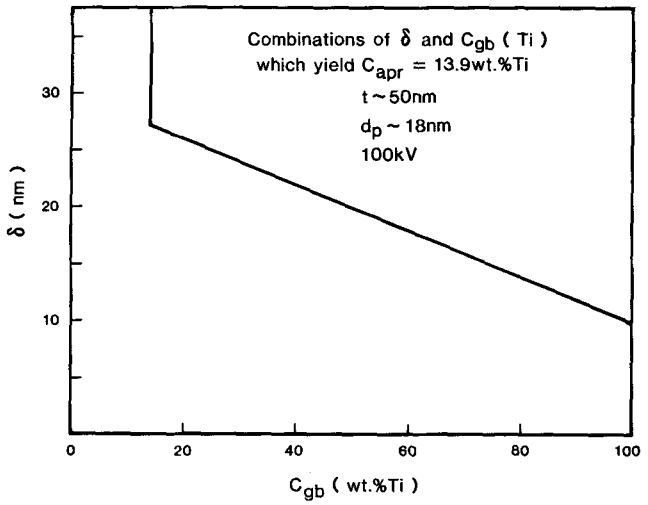


Fig. 17—Results of a calculation which show possible combinations of Ti-enriched layer thickness and level of Ti enrichment which yield a measured apparent Ti enrichment of 13.9 wt pct Ti for the present experimental conditions. Under these conditions, if the layer were thicker than approximately 27 nm, the layer composition could be measured directly. If the layer were thinner than 9.90 nm, even if it were pure Ti, the measured composition would be less than the apparent measured Ti enrichment of 13.9 wt pct Ti.

are shown in Figure 17. A curve similar to that shown in Figure 17 could be constructed for an apparent Ti concentration of 3.3 wt pct, the observed apparent concentration for the 1250 °C on-heating sample. Such a curve would allow one to determine combinations of Ti enrichment and enriched layer width which would yield the measured apparent concentration of 3.3 wt pct Ti. Without independent data to determine either the enriched layer composition or the thickness of the Ti-enriched layer, it is impossible to determine either from the measured apparent composition at the boundary. As AES was not performed on the 1250 °C on-heating sample fracture surface, it is not possible to determine the composition of the Ti-enriched layer which formed at the grain boundaries in this sample explicitly.

The value of the AEM, relative to AES, in examining grain boundary enrichment lies in the ability to examine many grain boundaries, including ones which did not liquate, and to correlate any observed elemental enrichment to other microstructural features, such as grain boundary precipitates.

The error associated with determining the composition of the enriched layer is due to many factors including X-ray counting statistics, accuracy of quantitation, determination of foil thickness, and the orientation of the enriched layer relative to the incident beam. The error analysis was performed by using the procedure described previously.[18] The X-ray counting error was taken to be three times the standard deviation ($3\sigma$). In the vicinity of the boundary, approximately 5000 Ti counts were obtained, yielding a counting statistic error of 4 pct. The quantitation error (accuracy of $k_{FeTi}$) was approximately 5 pct. The error in thickness determination is estimated to be 20 pct.[24] The error in misorientation of the boundary with respect to the electron beam is small relative to the other errors and was neglected.[18] Conservatively, the total relative error would be the sum of the individual relative errors or approximately 30 pct. The error bars shown on Figures 8, 9, and 14 were determined with this procedure.

## ACKNOWLEDGMENTS

The authors wish to acknowledge the assistance of W. R. Sorenson for performing the AEM analyses, R. E. Semarge for performing the electron microprobe analyses, and D. L. Humphreys for assistance with the data reduction and graphics support. The authors are also appreciative of the enlightening comments and discussion provided by the *Metallurgical Transactions* review committee. This work was performed at Sandia National Laboratories and supported by the United States Department of Energy under contract number DE-AC04-76DP00789.

## REFERENCES

1. D. A. Cononico, W. F. Savage, and G. M. Goodwin: *Proc. of Symposium Effects of Minor Elements on the Weldability of High-Nickel Alloys*, Welding Research Council, New York, NY, 1969, p. 68.
2. J. F. King and R. W. Reed, Jr.: ORNL Report No. TM-6276, 1976.
3. J. W. York and R. L. Flury: Westinghouse Electric Corporation, Tampa Division, Report No. WNET-119.
4. J. C. Lippold: *Welding Journal*, 1983, vol. 62, Research Supplement, p. 1.
5. "Incoloy Alloys 800, 800H, 801", Huntington Alloys Publication, 1978, p. 3.
6. J. J. Pepe and W. F. Savage: *Welding Journal*, 1967, vol. 46, Research Supplement, p. 411.
7. W. F. Savage and B. M. Krantz: *Welding Journal*, 1966, vol. 45, Research Supplement, p. 13.
8. W. A. Owczarski, D. S. Duvall, and C. P. Sullivan: *Welding Journal*,

1966, vol. 45, Research Supplement, p. 145.
9. D. S. Duvall and W. A. Owczarski: *Welding Journal*, 1967, Research Supplement, p. 423.
10. A. G. Vinckier: *Welding Journal*, 1971, vol. 50, Research Supplement, p. 19.
11. J. A. Brooks: *Welding Journal*, 1974, vol. 53, Research Supplement, p. 174s.
12. H. Tamura, N. Katayama, and T. Watanabe: *Trans. JWS*, 1974, vol. 5, p. 72.
13. W. F. Savage, E. F. Nippes, and T. W. Miller: *Welding Journal*, 1974, vol. 53, Research Supplement, p.181s.
14. J. M. Adamson, J. P. Adamson, and J. W. Martin: *Metallography*, 1972, vol. 5, p. 163.
15. J. A. Brooks and R. W. Krenzer: *Welding Journal*, 1974, vol. 53, Research Supplement, p. 242s.
16. A. D. Romig, Jr. and J. I. Goldstein: *Metall. Trans. A*, 1980, vol. 11A, p. 1151.
17. A. D. Romig, Jr. and M. J. Cieslak: *J. Appl. Phys.*, 1985, vol. 58, p. 3425.
18. J. R. Michael and D. B. Williams: *Metall. Trans. A*, 1984, vol. 15A, p. 99.
19. P. Doig, P. E. J. Flewitt, and R. K. Wild: *Philosph. Mag.*, 1978, vol. 37, p. 759.
20. *Analytical Electron Microscopy*, D. J. Joy, A. D. Romig, Jr., and J. I. Goldstein, eds., Plenum Press, New York, NY, 1986.
21. W. B. Jones and R. M. Allen: *Metall. Trans. A*, 1982, vol. 13A, p. 637.
22. *Gleeble 1500*, Duffers Scientific, Inc., R.D.#5, Box 85, Troy, NY 12180.
23. J. I. Goldstein, D. E. Newbury, P. Echlin, D. C. Joy, C. E. Fiori, and E. Lifshin: *Scanning Electron Microscopy and X-ray Microanalysis*, Plenum Press, New York, NY, 1981.
24. A. D. Romig, Jr. and M. J. Carr: *Analytical Electron Microscopy–1984*, D. B. Williams and D. C. Joy, eds., San Francisco Press, San Francisco, CA, 1984, p. 111.
25. G. Cliff and G. W. Lorimer: *Proc. 5th European Congress on Electron Microscopy*, Institute of Physics, London, 1972, p. 140.
26. J. I. Goldstein, J. L. Costley, G. W. Lorimer, and S. J. Reed: *SEM/1977*, O. Johari, ed., SEM Inc., Chicago, IL, 1977, p. 315.
27. B. Weiss, G. E. Grotke, and R. Stickler: *Welding Journal*, 1970, vol. 49, Research Supplement, p. 471.
28. W. F. Savage: *J. Appl. Polymer Sci.*, 1962, vol. 6, p. 303.
29. R. W. G. Wyckoff: *Crystal Structures*, 2nd ed., Wiley Interscience Publishers, New York, NY, 1963, p. 90.
30. A. D. Romig, Jr., D. E. Newbury, and R. L. Mykelbust: *Microbeam Analysis–1982*, K. F. J. Heinrich, ed., San Francisco Press, San Francisco, CA, 1982, p. 88.
31. H. Nahm and J. Moteff: *Metall. Trans. A*, 1976, vol. 7A, p. 1473.
32. J. Askill: *Tracer Diffusion Data for Metals, Alloys and Simple Oxides*, Plenum Press, New York, NY, 1970.
33. W. Jost: *Diffusion*, Academic Press, New York, NY, 1960.
34. M. Hansen: *Constitution of Binary Alloys*, McGraw-Hill, New York, NY, 1958, pp. 353, 670, 725.
35. W. F. Savage, E. F. Nippes, and M. C. Mushala: *Welding Journal*, 1978, vol. 57, Research Supplement, p. 237s.
36. S. J. Mathews and W. F. Savage: *Welding Journal*, 1971, vol. 50, Research Supplement, p. 174s.
37. J. W. Cahn: *Acta Metall.*, 1962, vol. 10, p. 789.
38. D. S. Duvall and W. A. Owczarski: *Welding Journal*, 1966, vol. 45, Research Supplement, p. 356.